# Extracting Trajectory Information from Two-Color Strong-Field Ionization

Nicolas Eicke* and Manfred Lein

Institut für Theoretische Physik, Leibniz Universität Hannover
Appelstraße 2, 30167 Hannover, Germany

**ARTICLE HISTORY**
Compiled November 24, 2016

**ABSTRACT**
Two-color ionization with a strong 800 nm field and a weak orthogonal 400 nm field allows for the retrieval of ionization times and relative amplitudes of short and long trajectories directly from the photoelectron momentum distribution by observing the signal as a function of the relative phase between the two fields. By numerical solution of the time-dependent Schrödinger equation in three dimensions we show that the amplitudes are strongly affected by Coulomb focusing. We determine these amplitudes as a function of the lateral momentum, revealing holographic structures in the delay scan.

**KEYWORDS**
strong-field ionization; electron trajectories; Coulomb focusing; photoelectron holography; intracycle interference

## 1. Introduction

Many effects in strong-field ionization of atoms and molecules can be understood in terms of electron trajectories [1, 2, 3]. An electron is removed from an atom at some ionization time and subsequently moves on a Newtonian trajectory in the laser field. Some of those trajectories return to the parent ion where they can rescatter elastically [4], or trigger high harmonic generation (HHG) [5, 6]. Electrons can absorb more photons than required to overcome the ionization threshold, which is known as above-threshold ionization (ATI) [7].

In ATI with a linearly polarized field, there are two fundamentally different kinds of trajectories. The long ATI trajectories originate in a descending quarter-cycle of the electric field and revisit the parent ion while the short ATI trajectories originate in the ascending quarter-cycle of the electric field and do not revisit[1]. Both kinds of trajectories can contribute to the same final momentum, leading to intracycle interference structures in the photoelectron momentum distribution [8, 9, 10]. This is also known as the attosecond double-slit [11]. The interference of scattered and non-scattered long trajectories leads to photoelectron holography [12, 13].

*Corresponding Author. Email: nicolas.eicke@itp.uni-hannover.de

[1] The distinction of trajectories by the terms 'short' and 'long' follows the usage in [8]. Note that this differs from the naming convention in HHG in the sense that both short and long HHG trajectories are long ATI trajectories.

Both insight into the ionization dynamics and control can be gained when combining the fundamental field with a second harmonic field, either with parallel or with orthogonal polarization. Dudovich and others used parallel 800/400 nm fields to determine recombination times in high harmonic generation [14]. Using orthogonal fields, it was also possible to measure ionization times [15, 16]. Further examples include the selection of different kinds of trajectories in HHG [17], phase-of-the-phase spectroscopy [18], spatial and temporal control of electron trajectories [19], studies on Coulomb effects [20] and the streaking double-slit experiment [21], where intracycle interference structures can be turned on and off.

The general idea common to the schemes using a strong field and a weak orthogonal field is that one can use the second field to distinguish contributions from different ionization times. In the HHG ionization time retrieval [15, 16], the presence of the second field favours a recollision of the returning electron only if ionization has taken place at a certain time that depends on the relative phase between the two fields. In the streaking double-slit experiment [21], short and long trajectories that would normally contribute to the same final momentum can be separated because their ionization times are not the same.

It was shown by numerical solution of the two-dimensional time-dependent Schrödinger equation (TDSE) that the orthogonal two-color scheme allows for the retrieval of ionization times for long trajectories and the determination of the relative amplitudes of short and long trajectories directly from the photoelectron momentum distribution [22]. The idea was that only trajectories with ionization times at a zero of the vector potential of the second harmonic field will end up having zero momentum in this direction. Thus scanning the on-axis signal (in direction of the fundamental field) as a function of the two-color delay and maximizing the signal at a given momentum, one can find the ionization times that contribute to photoelectrons with this particular momentum. As in the earlier works using HHG, it was found that the ionization times for the long trajectories are in good agreement with the quantum-orbit model [23, 24]. In the 2D calculations, the long trajectories dominate the on-axis signal with their amplitude being about twice as large as for the short trajectories.

In this paper we extend these results to three dimensions and show that the dominance of the long revisiting trajectories is enhanced due to Coulomb focusing [25]. Their signal is prominent in the delay scan almost up to the classical $2U_p$-limit for non-scattered electrons. This allows for a refinement of the ionization time retrieval and an extension to much higher momenta. Finally, we determine the relative amplitudes of short and long trajectories for nonzero lateral momentum by investigating the off-axis signal and we identify holographic structures in the delay scan. Atomic units are used throughout the article unless otherwise specified.

## 2. Computational details

We solve the three-dimensional single-active-electron TDSE in velocity gauge

$$i\frac{\partial}{\partial t}\psi(\mathbf{r},t) = \left(\frac{1}{2}\left(-i\nabla + \mathbf{A}(t)\right)^2 + V(\mathbf{r})\right)\psi(\mathbf{r},t) \tag{1}$$

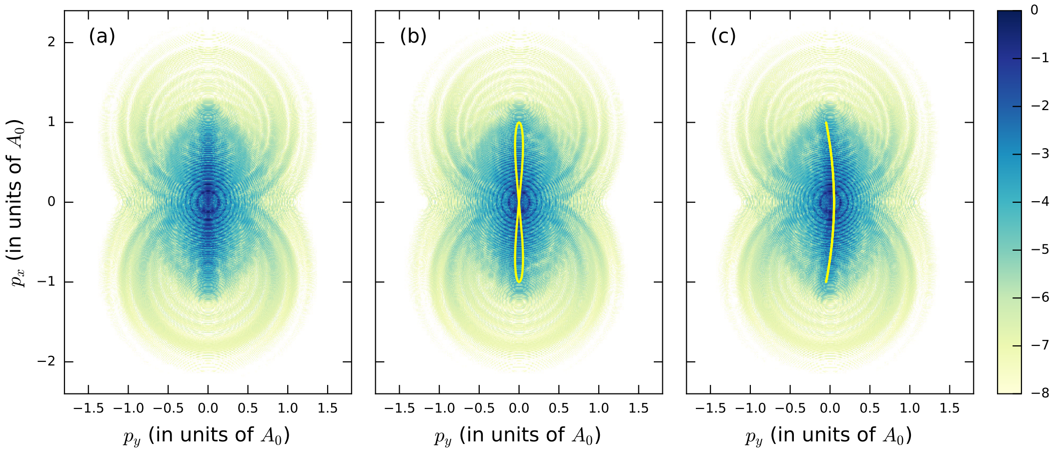


**Figure 1.** 2D slices through the 3D photoelectron momentum distribution at $p_z = 0$ ($\log_{10}$-scale, normalized such that the maximum value is one). (a) Single-color case. (b) Two-color case at $\phi = 0$. (c) Two-color case at $\phi = \pi/2$. The yellow lines represent $-\mathbf{A}(t)$. Momenta are in units of $A_0 = E_0/\omega$.

and obtain the photoelectron momentum distribution by projecting outgoing parts of the wave function on Volkov states [26]. Here,

$$V(\mathbf{r}) = -\frac{1 + e^{-\alpha r}}{\sqrt{\mathbf{r}^2 + 0.1}} \tag{2}$$

is a model soft-core potential with $\alpha$ optimized for the ground state to reproduce the ionization potential $I_p = 0.904\,\mathrm{a.u.}$ of helium. As in [22], the electric field $\mathbf{E}(t) = -\partial_t \mathbf{A}(t)$ is chosen as

$$\mathbf{E}(t) = E_0 f(t) \left(\cos(\omega t)\mathbf{e}_x + \epsilon \cos(2\omega t + \phi)\mathbf{e}_y\right) \tag{3}$$

with $E_0 = 0.107\,\mathrm{a.u.}$ corresponding to an intensity of $4 \times 10^{14}\,\mathrm{W/cm^2}$ and $\omega = 0.05695\,\mathrm{a.u.}$ corresponding to 800 nm wavelength. $f(t)$ is a trapezoidal envelope over two ascending, six constant and two descending cycles of the fundamental $\omega$-field. With $\epsilon = 0.1$, the relative field strength of the second harmonic field is weak compared to the fundamental field. $\phi$ denots the relative phase between the two fields. The wave function is propagated with the split-operator method [27] on a Cartesian grid with 768 points in each dimension over a length of 300 a.u. with a time step of 0.03 a.u. over a total propagation time of 1500 a.u.

## 3. Results and discussion

### 3.1. *Momentum distributions and on-axis signal*

Fig. 1 shows slices through the momentum distribution at zero lateral momentum ($p_z = 0$) for the single-color field and for the two-color field with different values of the delay phase $\phi$. Also shown is the curve described by the negative of the vector potential, $-\mathbf{A}(t)$, which is the final momentum of a classical photoelectron launched with zero velocity at time $t$. Depending on the relative phase $\phi$, the second harmonic

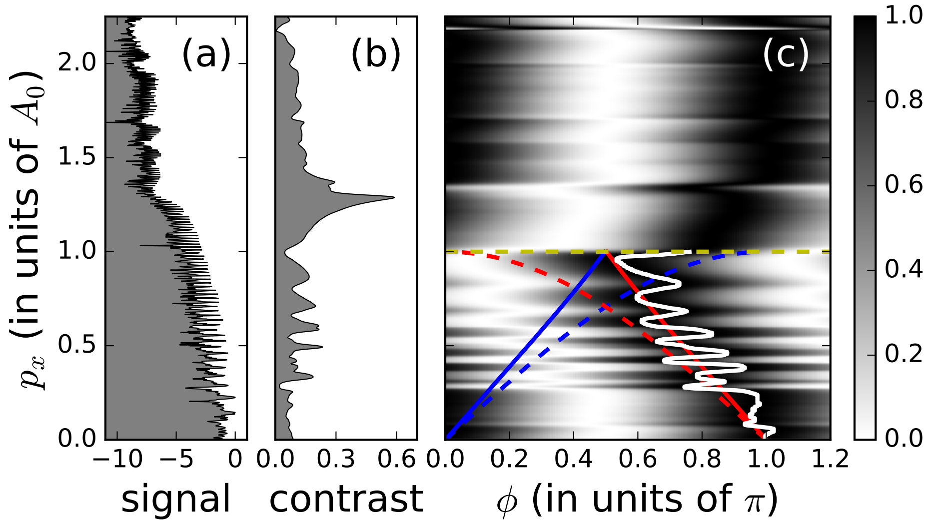


**Figure 2.** (a) On-axis TDSE photoelectron momentum distribution for the single-color 800 nm field. (b) Michelson contrast (defined as difference of highest and lowest value divided by their sum) of the dependence on the two-color delay phase $\phi$. (c) Variation of the signal as a function of the two-color delay phase $\phi$ and phases of maximum signal (white line). The red lines give the positions of maxima predicted by the quantum-orbit model (solid line) and the classical model (dashed line) for the long trajectories. Blue lines show the equivalent information for the short trajectories. For better visibility, the signal has been normalized for each $p_x$ to vary between zero and one. We have also applied a low-pass filter in the $p_x$ direction to remove spurious oscillations in the delay scan from the low signal between the ATI peaks. Therefore the ATI peak structure is not resolved in panels (b) and (c).

field affects short and long trajectories in a different way. For $\phi = 0$, short and long trajectories are deflected in opposite directions, while for $\phi = \pi/2$ they are deflected in the same direction, enhancing the visibility of intracycle interference structures as in the streaking double-slit experiment [21].

Next we concentrate on the photoelectrons with vanishing momentum component $p_y = 0$ in the direction of the second-harmonic field. Fig. 2(a) shows this on-axis signal for $p_x > 0$ in the single-color 800 nm field. Fig. 2(c) shows the variation as a function of the two-color delay phase $\phi$. The plotted signal is normalized for each $p_x$ separately so that the signal varies between zero and one. This representation clearly shows the $\phi$-dependence but it does not give information on its modulation depth. Therefore, the Michelson contrast is additionally shown in fig. 2(b). To interpret the results, fig. 2(c) includes the predictions for maximum signal made by the classical and the quantum-orbit model for the short and long trajectories. In the quantum-orbit model [23, 24], the saddle point equation

$$\frac{1}{2}\left(p_x + A_x(t_i)\right)^2 + I_p = 0 \tag{4}$$

gives for every momentum $p_x$ two complex ionization times $t_{\mathrm{short}}(p_x)$ and $t_{\mathrm{long}}(p_x)$ for the short and long trajectories respectively. Here, we have neglected the weak second-harmonic field. The maximum signal in each case is obtained when $\phi$ is chosen such that the real part of the transverse initial velocity vanishes,

$$\mathrm{Re}\, A_y(t_i(p_x), \phi) = 0. \tag{5}$$

The results for the classical model [1] are obtained by setting $I_p = 0$. As in [22], where the 2D TDSE was solved, we find that the positions of maximum signal agree well with the predictions made by the quantum-orbit model for the long trajectories. Moreover this agreement persists almost up to the classical limit $A_0 = E_0/\omega$ for non-scattered electrons, which was not the case in the earlier 2D analysis. We also find the oscillatory behavior that has previoulsy been explained as intracycle interferences of short and long trajectories and allowed for the relative amplitudes of those trajectories to be retrieved. To determine these trajectory weights from the 3D TDSE scan, we proceed as follows. Within the quantum-orbit model we write the semiclassical action (for $p_y = p_z = 0$)

$$S(p_x, t_i, \phi) = \int_0^{t_i} \mathrm{d}t \left[ \frac{1}{2} \left( p_x + A_x(t) \right)^2 + \frac{1}{2} A_y(t, \phi)^2 + I_p \right] \tag{6}$$

and associate complex amplitudes

$$a(p_x, \phi) = e^{iS(p_x, t_{\mathrm{short}}(p_x), \phi)} \tag{7}$$

and

$$b(p_x, \phi) = e^{iS(p_x, t_{\mathrm{long}}(p_x), \phi)} \tag{8}$$

with the short and long trajectories respectively. These amplitudes do not account for Coulomb focusing. It is expected, that Coulomb focusing increases the weight of the long trajectories in the on-axis signal. We therefore write the on-axis signal (up to a $p_x$-dependent normalization) as

$$\mathcal{M}(p_x, \phi) = \left| a(p_x, \phi) + \beta\, b(p_x, \phi) \right|^2 , \tag{9}$$

where $\beta$ gives the amplitude of the long trajectories relative to the short trajectories. We consider $\beta$ a complex number to allow for a phase shift between short and long trajectories. Such a shift is expected due to sub-barrier Coulomb effects [28, 29, 8]. We obtain $\beta$ by a least-squares fit in the intermediate momentum region ($0.4 < p_x/A_0 < 0.6$) of the curve of maximum signal from eq. (9) to the one from the TDSE, giving $|\beta| = 2.80$ as opposed to $|\beta| \approx 2.3$ from the 2D TDSE in [22].

Fig. 3 shows the signals obtained from the quantum-orbit model for the short trajectories, the long trajectories and the superposition with relative amplitude $\beta$. While the long trajectories give the correct positions for maximum signal on average, the superposition of both amplitudes is required to account for the oscillations. The strengths of these oscillations are governed by the relative amplitude.

### 3.2. *Dependence on lateral momentum*

So far, we have focused on the on-axis signal, i.e. $p_y = p_z = 0$. In the following, we keep $p_y = 0$ but we consider the signal along lines of non-zero lateral momentum $p_z$. Replacing $I_p \to I_p + p_z^2/2$ in eqs. (4) and (6) and repeating the analysis above, we can use the orthogonal two-color scheme to determine the relative amplitude $\beta$ of short and long trajectories for each $p_z$. Fig. 4 shows the absolute value and phase of $\beta$ as a function of $p_z$. We find that $\beta$ drops to $|\beta| \approx 1$ at $p_z \approx 0.12A_0$, indicating equal strength

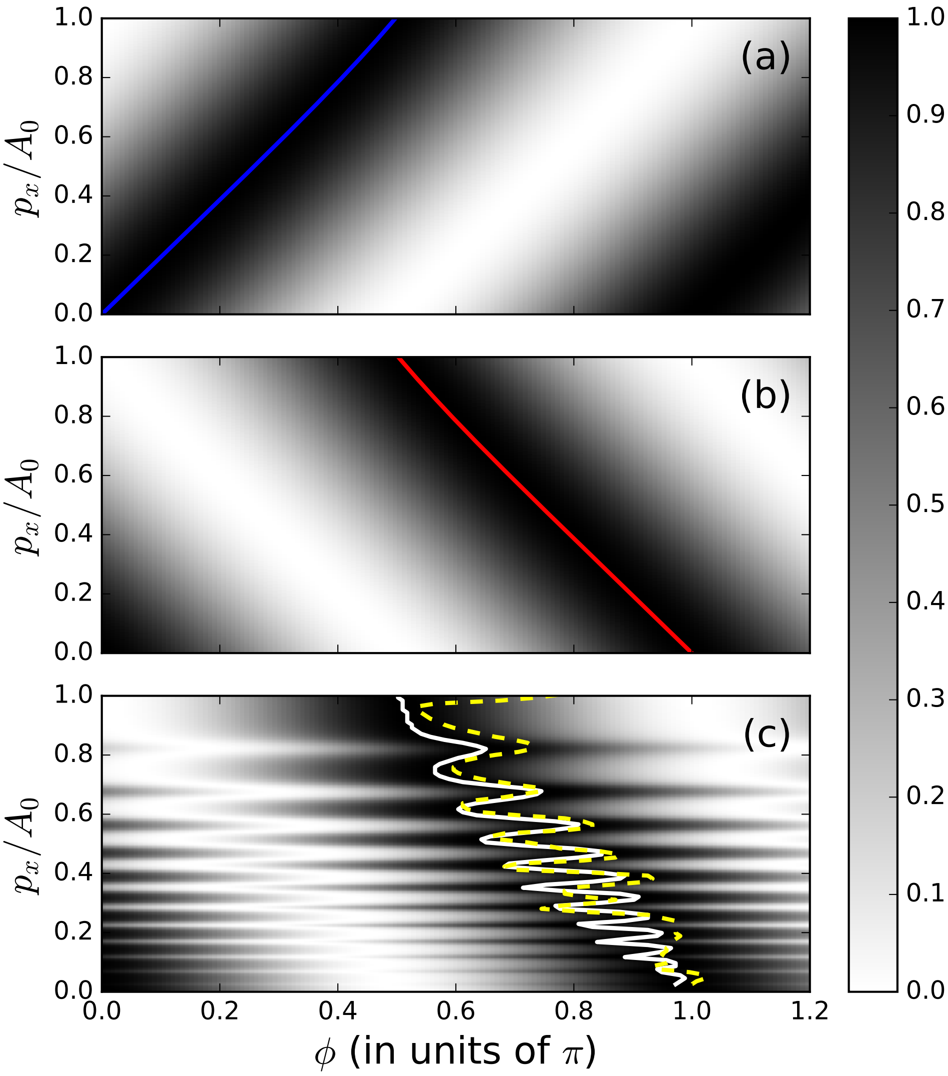


**Figure 3.** The figure illustrates the retrieval of the weights of short and long trajectories. (a) On-axis signal $|a|^2$ from the quantum-orbit model for the short trajectories as a function of the two-color delay. (b) On-axis signal $|b|^2$ for the long trajectories. (c) $|a + \beta b|^2$ for the total signal. The blue and red curves in (a), (b) are the same lines of maximum signal as in fig. 2. The white curve in (c) marks the maxima of the combined signal for optimized $\beta$ and the yellow (dashed) curve the TDSE result. As in fig. 2, the signals have been normalized to vary between zero and one.

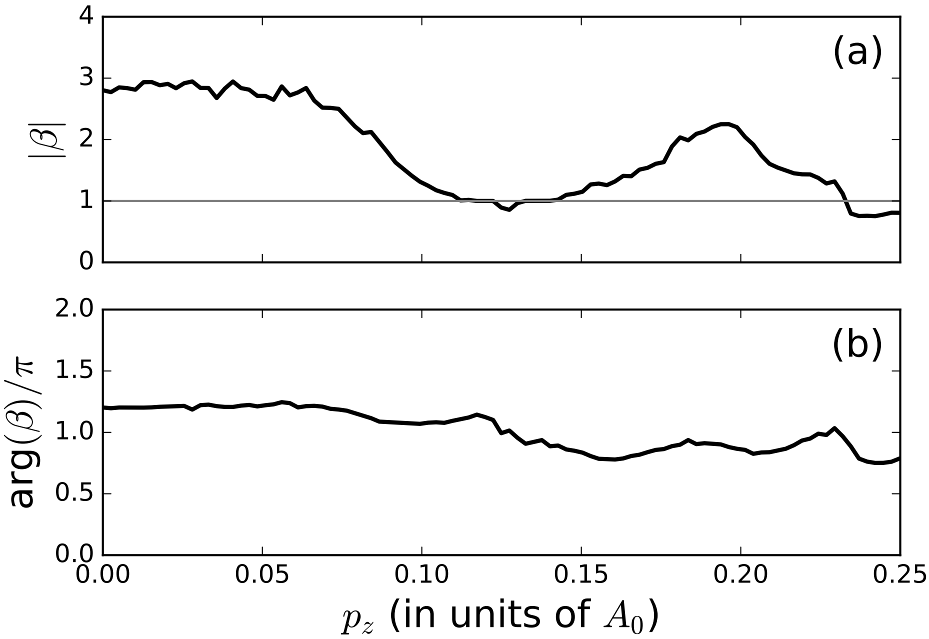


**Figure 4.** Lateral dependence of the absolute value (a) and phase shift (b) of the relative amplitude of short and long trajectories. Oscillations in the absolute value can be explained as holographic interferences in the signal from the long trajectories.

of both types of trajectories. However, there is a revival to $|\beta| \approx 2.2$ centered at $p_z \approx 0.19A_0$. These oscillations are due to photoelectron holography [12, 13]. While in the quantum-orbit model there is only one long trajectory for every momentum $(p_x, p_z)$, scattering in the ionic potential can refocus other trajectories to the same momentum. Thus $\beta$ can be viewed as the combined weight of two types of long trajectories, which correspond to the reference wave and scattered wave in holography. The oscillations in $\beta(p_z)$ are due to interference of these two types of long trajectories. This interpretation is further supported by the fact that the positions of minima and maxima agree well with the holographic structures visible in the momentum distribution in fig. 1 as the stripes that are almost parallel to the $p_x$-axis. We note that the phase of $\beta$ is only weakly dependent on the lateral momentum.

### 3.3. *Ionization times*

Finally, similar to the analysis in [22], we can reconstruct ionization times for long trajectories. First, we remove the oscillations in the delay-scan due to short trajectories by fitting a low-order polynomial to the curve of maximum signal in fig. 2 to get the positions of maximum signal $\phi_{\max}(p_x)$ for the long trajectories alone. Then, from the condition for maximum signal (5) we have

$$\mathrm{Re}(t_i) = \frac{n\pi - \phi_{\max}(p_x)}{2\omega}, \tag{10}$$

where in our case $n = 1$ selects the correct branch for long trajectories. The result is shown in fig. 5. Again we find that the ionization times agree well with the pre-

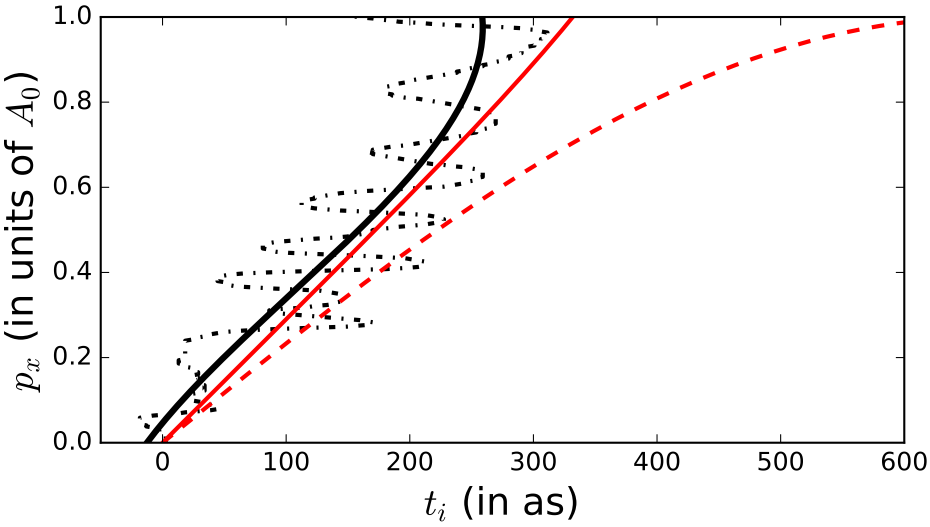


**Figure 5.** Ionization times for long trajectories from the two-color delay scan (black solid curve after removing oscillations and dotdashed curve before), the quantum-orbit model (red, solid) and the classical model (red, dashed). $t = 0$ marks the maximum of the electric field.

dictions made by the quantum-orbit model. Compared to the earlier 2D analysis, the agreement persists to much higher momenta. The reason for this is probably that with the increased strength of long trajectories due to Coulomb focusing, the influence of the trajectories forming the high-energy rescattering plateau is weaker and becomes important only at higher momenta.

## 4. Conclusion

We have used the orthogonal two-color scheme to extract relative amplitudes between short and long trajectories in ATI. In the direction of the strong field, long trajectories dominate the signal due to Coulomb focusing and are visible in the delay scan almost up to the classical $2U_p$-limit for non-scattered electrons. The delay dependence of the off-axis signal shows holographic structures. Moreover, two-color ATI offers a way to observe ionization times in strong-field photoionization with attosecond resolution, similar to the HHG scheme. In both cases, good agreement with the quantum-orbit model is found, but the analysis has been limited to the long trajectories. In the future, it might be interesting to identify regions of momentum space from which short-trajectory ionization times could be retrieved.

## 5. Acknowledgements


This work was supported by the Deutsche Forschungsgemeinschaft as part of the project *Momentum Distributions from Bichromatic Ionization of Atoms and Molecules* within the Priority Programme *Quantum Dynamics in Tailored Intense Fields* (QUTIF, SPP 1840).

## References


[1] Corkum, P.B.; Burnett, N.H.; Brunel, F. Above-threshold ionization in the long-wavelength limit, *Phys. Rev. Lett.* **1989**, *62*, 1259–1262. http://link.aps.org/doi/10.1103/PhysRevLett.62.1259.

[2] Corkum, P.B. Plasma perspective on strong field multiphoton ionization, *Phys. Rev. Lett.* **1993**, *71*, 1994–1997. http://link.aps.org/doi/10.1103/PhysRevLett.71.1994.

[3] Krause, J.L.; Schafer, K.J.; Kulander, K.C. High-order harmonic generation from atoms and ions in the high intensity regime, *Phys. Rev. Lett.* **1992**, *68*, 3535–3538. http://link.aps.org/doi/10.1103/PhysRevLett.68.3535.

[4] Paulus, G.G.; Nicklich, W.; Xu, H.; Lambropoulos, P.; Walther, H. Plateau in above threshold ionization spectra, *Phys. Rev. Lett.* **1994**, *72*, 2851–2854. http://link.aps.org/doi/10.1103/PhysRevLett.72.2851.

[5] McPherson, A.; Gibson, G.; Jara, H.; Johann, U.; Luk, T.S.; McIntyre, I.A.; Boyer, K.; Rhodes, C.K. Studies of multiphoton production of vacuum-ultraviolet radiation in the rare gases, *J. Opt. Soc. Am. B* **1987**, *4* (4), 595–601. http://josab.osa.org/abstract.cfm?URI=josab-4-4-595.

[6] Ferray, M.; L'Huillier, A.; Li, X.F.; Lompre, L.A.; Mainfray, G.; Manus, C. Multiple-harmonic conversion of 1064 nm radiation in rare gases, *Journal of Physics B: Atomic, Molecular and Optical Physics* **1988**, *21* (3), L31. http://stacks.iop.org/0953-4075/21/i=3/a=001.

[7] Agostini, P.; Fabre, F.; Mainfray, G.; Petite, G.; Rahman, N.K. Free-Free Transitions Following Six-Photon Ionization of Xenon Atoms, *Phys. Rev. Lett.* **1979**, *42*, 1127–1130. http://link.aps.org/doi/10.1103/PhysRevLett.42.1127.

[8] Yan, T.M.; Bauer, D. Sub-barrier Coulomb effects on the interference pattern in tunneling-ionization photoelectron spectra, *Phys. Rev. A* **2012**, *86*, 053403. http://link.aps.org/doi/10.1103/PhysRevA.86.053403.

[9] Arbó, D.G.; Persson, E.; Burgdörfer, J. Time double-slit interferences in strong-field tunneling ionization, *Phys. Rev. A* **2006**, *74*, 063407. http://link.aps.org/doi/10.1103/PhysRevA.74.063407.

[10] Arbó, D.G.; Ishikawa, K.L.; Schiessl, K.; Persson, E.; Burgdörfer, J. Intracycle and intercycle interferences in above-threshold ionization: The time grating, *Phys. Rev. A* **2010**, *81*, 021403. http://link.aps.org/doi/10.1103/PhysRevA.81.021403.

[11] Lindner, F.; Schätzel, M.G.; Walther, H.; Baltuška, A.; Goulielmakis, E.; Krausz, F.; Milošević, D.B.; Bauer, D.; Becker, W.; Paulus, G.G. Attosecond Double-Slit Experiment, *Phys. Rev. Lett.* **2005**, *95*, 040401. http://link.aps.org/doi/10.1103/PhysRevLett.95.040401.

[12] Huismans, Y.; Rouzée, A.; Gijsbertsen, A.; Jungmann, J.H.; Smolkowska, A.S.; Logman, P.S.W.M.; Lépine, F.; Cauchy, C.; Zamith, S.; Marchenko, T.; et al. Time-Resolved Holography with Photoelectrons, *Science* **2011**, *331* (6013), 61–64. http://science.sciencemag.org/content/331/6013/61.

[13] Bian, X.B.; Huismans, Y.; Smirnova, O.; Yuan, K.J.; Vrakking, M.J.J.; Bandrauk, A.D. Subcycle interference dynamics of time-resolved photoelectron holography with midinfrared laser pulses, *Phys. Rev. A* **2011**, *84*, 043420. http://link.aps.org/doi/10.1103/PhysRevA.84.043420.

[14] Dudovich, N.; Smirnova, O.; Levesque, J.; Mairesse, Y.; Ivanov, M.Y.; Villeneuve, D.M.; Corkum, P.B. Measuring and controlling the birth of attosecond XUV pulses, *Nat. Phys.* **2006**, *2* (11), 781–786. http://dx.doi.org/10.1038/nphys434.

[15] Shafir, D.; Soifer, H.; Bruner, B.D.; Dagan, M.; Mairesse, Y.; Patchkovskii,

S.; Ivanov, M.Y.; Smirnova, O.; Dudovich, N. Resolving the time when an electron exits a tunnelling barrier, *Nature* **2012**, *485* (7398), 343–346. http://dx.doi.org/10.1038/nature11025.

[16] Zhao, J.; Lein, M. Determination of Ionization and Tunneling Times in High-Order Harmonic Generation, *Phys. Rev. Lett.* **2013**, *111*, 043901. http://link.aps.org/doi/10.1103/PhysRevLett.111.043901.

[17] Brugnera, L.; Hoffmann, D.J.; Siegel, T.; Frank, F.; Zaïr, A.; Tisch, J.W.G.; Marangos, J.P. Trajectory Selection in High Harmonic Generation by Controlling the Phase between Orthogonal Two-Color Fields, *Phys. Rev. Lett.* **2011**, *107*, 153902. http://link.aps.org/doi/10.1103/PhysRevLett.107.153902.

[18] Skruszewicz, S.; Tiggesbäumker, J.; Meiwes-Broer, K.H.; Arbeiter, M.; Fennel, T.; Bauer, D. Two-Color Strong-Field Photoelectron Spectroscopy and the Phase of the Phase, *Phys. Rev. Lett.* **2015**, *115*, 043001. http://link.aps.org/doi/10.1103/PhysRevLett.115.043001.

[19] Zhang, L.; Xie, X.; Roither, S.; Kartashov, D.; Wang, Y.; Wang, C.; Schöffler, M.; Shafir, D.; Corkum, P.B.; Baltuška, A.; et al. Laser-sub-cycle two-dimensional electron-momentum mapping using orthogonal two-color fields, *Phys. Rev. A* **2014**, *90*, 061401. http://link.aps.org/doi/10.1103/PhysRevA.90.061401.

[20] Richter, M.; Kunitski, M.; Schöffler, M.; Jahnke, T.; Schmidt, L.P.H.; Dörner, R. Ionization in orthogonal two-color laser fields: Origin and phase dependences of trajectory-resolved Coulomb effects, *Phys. Rev. A* **2016**, *94*, 033416. http://link.aps.org/doi/10.1103/PhysRevA.94.033416.

[21] Richter, M.; Kunitski, M.; Schöffler, M.; Jahnke, T.; Schmidt, L.P.H.; Li, M.; Liu, Y.; Dörner, R. Streaking Temporal Double-Slit Interference by an Orthogonal Two-Color Laser Field, *Phys. Rev. Lett.* **2015**, *114*, 143001. http://link.aps.org/doi/10.1103/PhysRevLett.114.143001.

[22] Henkel, J.; Lein, M. Analysis of electron trajectories with two-color strong-field ionization, *Phys. Rev. A* **2015**, *92*, 013422. http://link.aps.org/doi/10.1103/PhysRevA.92.013422.

[23] Salières, P.; Carré, B.; Le Déroff, L.; Grasbon, F.; Paulus, G.G.; Walther, H.; Kopold, R.; Becker, W.; Milošević, D.B.; Sanpera, A.; et al. Feynman's Path-Integral Approach for Intense-Laser-Atom Interactions, *Science* **2001**, *292* (5518), 902–905. http://science.sciencemag.org/content/292/5518/902.

[24] Milošević, D.B.; Paulus, G.G.; Bauer, D.; Becker, W. Above-threshold ionization by few-cycle pulses, *Journal of Physics B: Atomic, Molecular and Optical Physics* **2006**, *39* (14), R203. http://stacks.iop.org/0953-4075/39/i=14/a=R01.

[25] Brabec, T.; Ivanov, M.Y.; Corkum, P.B. Coulomb focusing in intense field atomic processes, *Phys. Rev. A* **1996**, *54*, R2551–R2554. http://link.aps.org/doi/10.1103/PhysRevA.54.R2551.

[26] Lein, M.; Gross, E.K.U.; Engel, V. Intense-Field Double Ionization of Helium: Identifying the Mechanism, *Phys. Rev. Lett.* **2000**, *85*, 4707–4710. http://link.aps.org/doi/10.1103/PhysRevLett.85.4707.

[27] Feit, M.D.; Fleck, J.A. Solution of the Schrdinger equation by a spectral method II: Vibrational energy levels of triatomic molecules, *The Journal of Chemical Physics* **1983**, *78*, 301–308. http://scitation.aip.org/content/aip/journal/jcp/78/1/10.1063/1.444501.

[28] Arbó, D.G.; Nagele, S.; Tong, X.M.; Xie, X.; Kitzler, M.; Burgdörfer, J. Interference of electron wave packets in atomic ionization by subcycle sculpted laser pulses, *Phys. Rev. A* **2014**, *89*, 043414. http://link.aps.org/doi/10.1103/PhysRevA.89.043414.

[29] Arbó, D.G. The effect of the Coulomb potential on subcycle interference of electron wave packets in atomic ionization by two-colour laser pulses, *Journal of Physics B: Atomic, Molecular and Optical Physics* **2014**, *47* (20), 204008. http://stacks.iop.org/0953-4075/47/i=20/a=204008.